

# Journal of Materials Chemistry A

Accepted Manuscript



This is an *Accepted Manuscript*, which has been through the Royal Society of Chemistry peer review process and has been accepted for publication.

*Accepted Manuscripts* are published online shortly after acceptance, before technical editing, formatting and proof reading. Using this free service, authors can make their results available to the community, in citable form, before we publish the edited article. We will replace this *Accepted Manuscript* with the edited and formatted *Advance Article* as soon as it is available.

You can find more information about *Accepted Manuscripts* in the [Information for Authors](#).

Please note that technical editing may introduce minor changes to the text and/or graphics, which may alter content. The journal's standard [Terms & Conditions](#) and the [Ethical guidelines](#) still apply. In no event shall the Royal Society of Chemistry be held responsible for any errors or omissions in this *Accepted Manuscript* or any consequences arising from the use of any information it contains.

## ARTICLE

# Preparation of $\text{Co}_3\text{O}_4$ electrode materials with different microstructures *via* pseudomorphic conversion of Co-based metal-organic frameworks

Cite this: DOI: 10.1039/x0xx00000x

Kyung Joo Lee,<sup>a‡</sup> Tae-Hee Kim,<sup>b‡</sup> Tae Kyung Kim,<sup>a</sup> Jae Hwa Lee,<sup>a</sup> Hyun-Kon Song,<sup>\*b</sup> and Hoi Ri Moon<sup>\*a</sup>

Received 00th January 2012,  
Accepted 00th January 2012

DOI: 10.1039/x0xx00000x

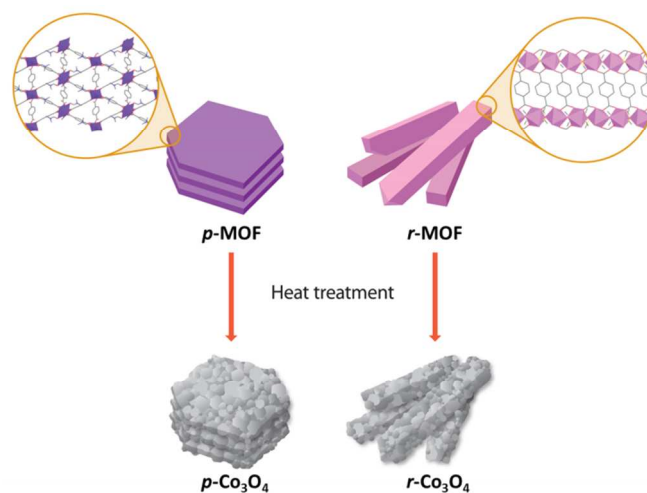
www.rsc.org/

To develop high-performance nanostructured metal oxide electrodes, it is important to understand the structural effects on electrochemical performances. Thus, the preparation of metal oxide materials which have well-tailored nanostructures is crucial for the studies. However, while the synthetic strategies to control the size of metal oxide nanoparticles are well-developed, the control of those higher level structures, namely microstructure, is not established very well. Herein, we present the synthesis of two kinds of  $\text{Co}_3\text{O}_4$  nanomaterials through pseudomorphic conversion that the macroscopic morphologies of parent MOFs such as plate-like and rod-like shape were well-maintained. Both  $\text{Co}_3\text{O}_4$  nanomaterials are composed of almost identical 10 nm-sized primary nanocrystals, but those nanoporous secondary structures and macroscopic morphologies such as plate and rod shapes are different. Those  $\text{Co}_3\text{O}_4$  nanomaterials were utilized as an electrode of lithium ion batteries (LIBs), and their electrochemical properties were comparatively studied. It was revealed that the different cyclability and rate capability are attributed to their different microstructures. Pseudo-monolithic integration of the primary and secondary structures at higher level was the governing factor to determine the electrochemical performances of the  $\text{Co}_3\text{O}_4$ .

## Introduction

Metal-organic frameworks (MOFs) with diverse structures can be synthesized by introducing various building blocks and using different conditions.<sup>1</sup> Since the structures of MOFs govern their intrinsic properties,<sup>2</sup> much effort has been made to synthesize such materials for applications to gas storage and separation,<sup>3-4</sup> sensing,<sup>5</sup> and catalysis.<sup>6</sup> Another emerging avenue of MOF research is aimed at utilizing these materials for the synthesis of metal or metal oxide nanomaterials via thermolysis.<sup>7-11</sup> Ordered metal clusters coordinated by organic linkers in MOF crystals can act as useful materials for the synthesis of uniformly small-sized and well-dispersed metal or metal oxide nanoparticles. Organic linkers not only prevent aggregation of nanoparticles during thermolysis, they also impart porosity to the resultant nanostructures after their removal.

MOF-derived metal oxide nanocomposites are utilized as electrode materials for energy storage and conversion. The Cho group reported the use of MIF-88-Fe synthesis as a precursor for the synthesis of nanoporous spindle-like  $\alpha\text{-Fe}_2\text{O}_3$ , which functions as an improved electrode material for lithium ion batteries (LIBs). This material was composed of 20 nm-sized



**Scheme 1.** Scheme of pseudomorphic conversion of Co-MOFs.

primary nanoparticles, resulting in a nanoporous secondary structure.<sup>9</sup> Ogale *et al.* synthesized CuO nanostructures from a Cu-based MOF under an air atmosphere. The samples, which had a highly aggregated particulate morphology of ca. 40 nm CuO nanoparticles, displayed good electrochemical performances as an anode for LIBs.<sup>10</sup> By pyrolyzing  $[\text{Co}_3(\text{NDC})_3(\text{DMF})_4]_n$  (NDC= 2,6-naphthalenedicarboxylate;

DMF= *N,N*-dimethylformamide), Xu *et al.* synthesized agglomerated secondary structures with an average diameter of around 250 nm, which contained primary Co<sub>3</sub>O<sub>4</sub> nanoparticles with a size of about 25 nm. This agglomerated Co<sub>3</sub>O<sub>4</sub> material exhibited enhanced capacities and cyclability as an electrode material for LIB.<sup>11</sup> Examples such as these illustrate that the development of metal oxide nanostructures as electrode materials for LIBs has largely remained focused on the use of primary nanoparticles and their agglomerated particles.

In addition to the effects of primary nanoparticles and secondary structures on electrochemical performances, it is worthwhile to investigate tertiary architectures between 10 to 100 μm as the highest level, which correspond to macroscopic shapes. Electric and ionic pathways to redox-active sites of the primary particles are determined by the secondary structure.<sup>12-15</sup> Tight integration of the secondary structures is also crucial for enhanced charge transfer if other conductive agents are not present between the secondary agglomerates. Therefore, an important means of maximizing electrochemical performance involves the integration of secondary structures, which serves to influence tertiary structure. To the best of our knowledge, there are no reported comparison studies of metal oxide electrode materials having different macroscopic morphologies. Proper heat treatment of MOFs leads to pseudomorphic conversion with retention of the parent MOF morphology. In other words, metal oxide nanostructures composed of the same primary particles, but with different secondary or tertiary architecture, can be generated via pyrolysis of MOFs. By implementing this approach, the synthesis of two different MOFs comprising the same building blocks can provide an opportunity to study how macroscopic structure affects practical application.

Herein, we report the synthesis of two kinds of Co<sub>3</sub>O<sub>4</sub> nanomaterials through pseudomorphic conversion wherein the macroscopic morphologies of parent MOFs were well-maintained (Scheme 1). We successfully synthesized both plate-shaped ([Co<sub>3</sub>(BDC)<sub>3</sub>(DMF)<sub>4</sub>]<sub>*n*</sub>, *p*-MOF) and rod-shaped ([Co(BDC)(DMSO)]<sub>*n*</sub>, *r*-MOF) Co-MOFs, which are constructed from the same Co<sup>2+</sup> ions and 1,4-benzenedicarboxylate (BDC) ligands. After optimized thermolysis, the Co-MOFs were transformed into Co<sub>3</sub>O<sub>4</sub> materials having plate-like (*p*-Co<sub>3</sub>O<sub>4</sub>) or rod-like (*r*-Co<sub>3</sub>O<sub>4</sub>) morphologies, respectively. The electrochemical performances of these Co<sub>3</sub>O<sub>4</sub> materials as LIB electrodes were examined with the respect to metal oxide microstructure.

## Experimental section

### Materials and characterizations

All chemicals and solvents were of reagent grade and used without further purification. Infrared spectra were recorded with a ThermoFisher Scientific iS10 FT-IR spectrometer. Elemental analyses (for C, H, N, S, and O) were performed using a Thermo Scientific Flash 2000 series CHNS/O analyzer.

Thermogravimetric analysis (TGA) was performed under N<sub>2</sub> (g) at a scan rate of 5 °C min<sup>-1</sup>, using a TGA Q50 from TA Instruments. Transmission electron microscope (TEM) images were obtained with a JEOL JEM-2100F microscope. X-ray powder diffraction (XRPD) data of as-synthesized MOFs were recorded at the Pohang Accelerator Laboratory, Korea. To obtain the XRPD patterns, the well-ground powders of as-synthesized MOFs were loaded into the capillaries, respectively (diameter, 0.3 mm; wall thickness, 0.01 mm). Diffraction data were collected at room temperature with detector distance of 180 mm and 60 s exposures using synchrotron radiation ( $\lambda = 1.20024 \text{ \AA}$ ) on an ADSC Quantum-210 detector at 2D SMC with a silicon (111) double-crystal monochromator (DCM). The *ADS* program<sup>16</sup> was used for data collection, and the *Fit2D*<sup>17</sup> program was used to convert a two-dimensional diffraction image to a one-dimensional diffraction pattern. X-ray powder diffraction (XRPD) data of *p*-Co<sub>3</sub>O<sub>4</sub> and *r*-Co<sub>3</sub>O<sub>4</sub> were recorded on a Bruker D8 advance diffractometer at 40 kV and 40 mA and a Bruker D2 phaser diffractometer at 30 kV and 10 mA for Cu K $\alpha$  ( $\lambda = 1.541 \text{ \AA}$ ), with a step size of 0.02° in 2 $\theta$ . N<sub>2</sub> sorption isotherms of *p*-Co<sub>3</sub>O<sub>4</sub> and *r*-Co<sub>3</sub>O<sub>4</sub> were obtained by BELSORP-max at 77 K. Prior to the adsorption measurements, both samples were evacuated ( $p < 10^{-5}$  mbar) at 200 °C for 6 h. The specific surface area was determined in the relative pressure range from 0.05 to 0.3 of the Brunauer-Emmett-Teller (BET) plot, and the total pore volume was calculated from the amount adsorbed at a relative pressure of about 0.98-0.99.

### Single-crystal X-ray crystallography

Single crystals of *p*-MOF and *r*-MOF coated with paratone-N oil were mounted on a loop. Diffraction data of *p*-MOF were collected at 100 K with synchrotron radiation ( $\lambda = 0.70002 \text{ \AA}$ ) on an ADSC Quantum-210 detector at 2D SMC with a silicon(111) DCM at the Pohang Accelerator Laboratory, Korea. The ADSC Q210 *ADX* program<sup>16</sup> was used for data collection, and HKL3000sm (Ver. 703r)<sup>18</sup> was used for cell refinement, reduction, and absorption correction. Diffraction data of *r*-MOF were collected at 173 K using a Rigaku R-ax Rapid II diffractometer (Mo K $\alpha$   $\lambda = 0.71073 \text{ \AA}$ ), equipped with a diffraction camera system and an imaging plate. Full sphere data were collected for all crystals, and the raw data were processed and scaled using the RapidAuto software suite.<sup>19</sup> The crystal structures of *p*-MOF and *r*-MOF were solved by direct methods and refined by full-matrix least-squares refinement using the SHELXL-97 computer program<sup>20</sup> for *p*-MOF and SHELX-TL (Ver. 2008) program package<sup>21</sup> for *r*-MOF. The positions of all non-hydrogen atoms were refined with anisotropic displacement factors. The hydrogen atoms were positioned geometrically using a riding model. Relevant crystallographic data and bond lengths (Å) and angles (°) for *p*-MOF and *r*-MOF are summarized in Table S1-S4.

### Synthesis of plate-shaped Co-MOF ([Co<sub>3</sub>(BDC)<sub>3</sub>(DMF)<sub>4</sub>]<sub>*n*</sub>, *p*-MOF)

H<sub>2</sub>BDC (29 mg, 0.17 mmol) and adipic acid (37 mg, 0.25 mmol) were dissolved in DMF (3 mL), and mixed with a DMF solution (2 mL) of Co(NO<sub>3</sub>)<sub>2</sub>·6H<sub>2</sub>O (99 mg, 0.34 mmol). The solution was sealed in a glass jar, heated to 100 °C for 24 h, and then cooled to room temperature. Purple plate-shaped crystals formed, which were filtered and washed briefly with fresh DMF. Yield: 51 mg (94% based on H<sub>2</sub>BDC). Anal. Calcd for Co<sub>3</sub>C<sub>36</sub>H<sub>40</sub>N<sub>4</sub>O<sub>16</sub>: C, 44.97; H, 4.19; N, 5.83. Found: C, 44.51; H, 4.55; N, 6.44. FT-IR (KBr, cm<sup>-1</sup>): ν<sub>O-H</sub>, 3417(br); ν<sub>C-H( aromatic)</sub>, 3072(w); ν<sub>C=O(DMF)</sub>, 1650(s); ν<sub>O-C=O(carboxylate)</sub>, 1609, 1385(s); ν<sub>C=C( aromatic ring)</sub>, 1502(w).

#### Synthesis of rod-shaped Co-MOF ([Co(BDC)(DMSO)]<sub>n</sub>, *r*-MOF)

Co(NO<sub>3</sub>)<sub>2</sub>·6H<sub>2</sub>O (99 mg, 0.34 mmol) was dissolved in DMF (2 mL), and mixed with a DMSO (3 mL) solution of H<sub>2</sub>BDC (40 mg, 0.24 mmol). The solution was kept in a glass-jar at 120 °C for 24 h, and then cooled to room temperature. Pink rod-shaped crystals formed, which were filtered, and washed briefly with fresh DMSO. Yield: 44 mg (60% based on H<sub>2</sub>BDC). Anal. Calcd for Co<sub>1</sub>C<sub>10</sub>H<sub>10</sub>S<sub>1</sub>O<sub>5</sub>: C, 39.88; H, 3.35; N, 0.00; S, 10.65. Found: C, 39.88; H, 3.33; N, 0.06; S, 11.84. FT-IR (KBr, cm<sup>-1</sup>): ν<sub>O-H</sub>, 3431(br); ν<sub>C-H( aromatic)</sub>, 3073, 3016(w); ν<sub>O-C=O(carboxylate)</sub>, 1579, 1392(s); ν<sub>C=C( aromatic ring)</sub>, 1498(w); ν<sub>S=O( coordinating DMSO)</sub>, 943(s).

#### Synthesis of plate-shaped Co<sub>3</sub>O<sub>4</sub> (*p*-Co<sub>3</sub>O<sub>4</sub>)

As-synthesized *p*-MOF (1.02 g) was heated at a rate of 5 °C min<sup>-1</sup> under N<sub>2</sub> (g) flow of 50 mL min<sup>-1</sup>. The material was maintained at the target temperature of 440 °C for 12 h. After cooling to room temperature, the second heat treatment to completely transform into Co<sub>3</sub>O<sub>4</sub> was performed under O<sub>2</sub> (g) flow of 0.1 L min<sup>-1</sup> and heated at a rate of 5 °C min<sup>-1</sup>. The material was maintained at the target temperature of 350 °C for 1 h. After cooling to room temperature, black solid (0.245 g) was obtained.

#### Synthesis of rod-shaped Co<sub>3</sub>O<sub>4</sub> (*r*-Co<sub>3</sub>O<sub>4</sub>)

As-synthesized *r*-MOF (0.83 g) was heated at a rate of 5 °C min<sup>-1</sup> under N<sub>2</sub> (g) flow of 50 mL min<sup>-1</sup>. The material was maintained at the target temperature of 500 °C of 1 h. After cooling to room temperature, the second heat treatment completely transform into Co<sub>3</sub>O<sub>4</sub> was performed under O<sub>2</sub> (g) flow of 0.1 L min<sup>-1</sup> and heated at a rate of 5 °C min<sup>-1</sup>. After reaching the target temperature of 500 °C, the material was maintained at that temperature for 1 h. After cooling to room temperature, black solid (0.20 g) was obtained.

#### Electrochemical measurements

The electrochemical properties of *p*-Co<sub>3</sub>O<sub>4</sub> and *r*-Co<sub>3</sub>O<sub>4</sub> were characterized using coin-type cells (CR2032) assembled in an Ar-filled glove box. The electrodes were fabricated by mixing the cobalt oxide powders (*p*-Co<sub>3</sub>O<sub>4</sub> or *r*-Co<sub>3</sub>O<sub>4</sub>) with polyvinylidene fluoride (PVDF) as a binder and with Super P as

a conducting agent at a weight ratio of 8:1:1 in *N*-methyl-2-pyrrolidinone solvent. The slurry was cast onto Cu foil and then dried in a vacuum oven at 120 °C for 2 h. A piece of polyolefin membrane, used as a separator was placed between a piece of electrode and Li metal, used as a counter electrode. Cell assembly is visually described in Fig. S1. A 1 M solution of LiPF<sub>6</sub> in a mixture of ethylene carbonate (EC) and diethyl carbonate (DEC) at 1:1 v/v was used as an electrolyte. All of the assembled coin cells were initially lithiated to 0.001 V at 0.1C and then delithiated up to 3 V at the same rate. The conditions for the following galvanostatic lithiation and delithiation were indicated in figure captions in electrochemical tests for measuring cyclability and rate capability. 1C was defined as 890 mA g<sup>-1</sup>, considering the theoretical capacity calculated based on the conversion reaction of Co<sub>3</sub>O<sub>4</sub> into Co and LiO<sub>2</sub> (890 mAh g<sup>-1</sup>).

#### Results and Discussion

To synthesize two different MOFs composed of the same building blocks for the comparative studies, Co<sup>2+</sup> and BDC ligands were reacted under different conditions. Previous reports showed that the solvothermal reaction of Co<sup>2+</sup> ions and BDC ligands in amide solutions produced mainly the anionic MOF structures possessing protonated dimethylamines counterions.<sup>22-24</sup> The group of Yaghi reported a MOF structure composed Co<sup>2+</sup> and BDC,<sup>25</sup> but the reaction conditions employed produced a mixture of products, which required a physical separation process in order to obtain a pure phase. In the present work, we successfully optimized the synthetic conditions for two MOFs composed of Co<sup>2+</sup> and BDC ligands having either plate-like and rod-like crystal morphologies.

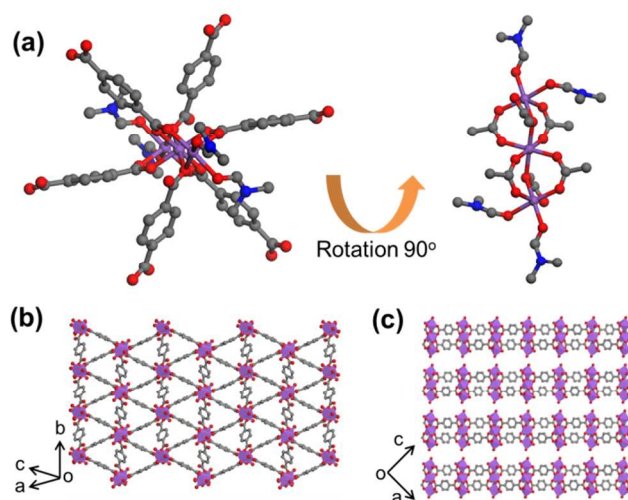


**Fig. 1** Single-crystal X-ray structure of *p*-MOF. (a) The SBU of the Co<sub>3</sub>(COO)<sub>6</sub> cluster. (b) 2D layered structure of *p*-MOF. (c) 3D structure formed by stacking of the 2D layers. Colour scheme: Co, purple; C, grey; O, red; N, blue.

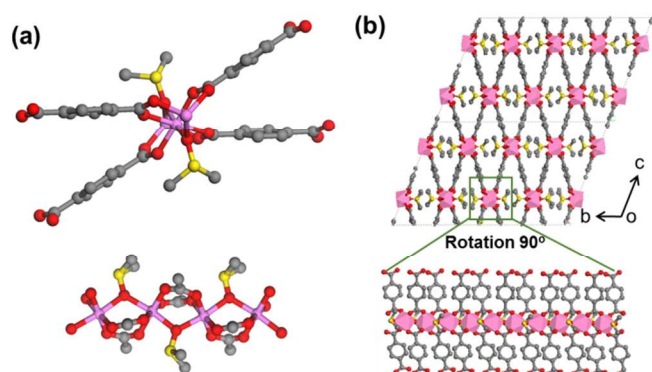


**Fig. 2** Single-crystal X-ray structure of *r*-MOF. (a) The SBU of the Co-O chain. (b) The *bc* plane of the 3D network, which is constructed by association of the SBUs and BDC ligands. Colour scheme: Co, pink; C, grey; O, red; S, yellow.

The purple plate-shaped MOF (*p*-MOF) crystals of  $[\text{Co}_3(\text{BDC})_3(\text{DMF})_4]_n$  were synthesized from a DMF solution of  $\text{Co}(\text{NO}_3)_2 \cdot 6\text{H}_2\text{O}$  and two kinds of ligands,  $\text{H}_2\text{BDC}$  and adipic acid via a solvothermal reaction. As shown in Fig. 1a and Fig. S2, adipic acid was not contained within the structure of *p*-MOF, and might instead act as a structure-directing agent for the formation of *p*-MOF. The same reaction performed without adipic acid yielded a mixture of purple microcrystals and powdery products, which were not appropriate for X-ray structural analysis. The *p*-MOF possesses two crystallographically independent cobalt atoms in distorted octahedral and distorted trigonal bipyramidal coordination geometries. Two 5-coordinate  $\text{Co}^{2+}$  ions and one 6-coordinate  $\text{Co}^{2+}$  ion form a  $\text{Co}_3(\text{COO})_6$  cluster as a secondary building unit (SBU) by coordination with BDC ligands. Since two ends of the  $\text{Co}_3$  cluster are terminated by coordinated DMF molecules, the SBUs are interconnected by BDC ligands resulting in 2D layers extended in the (10-1) plane (Fig. 1b), which are infinitely stacked in the [101] direction (Fig. 1c). The X-ray powder diffraction (XRPD) pattern of *p*-MOF showed good agreement with the simulated pattern (Fig. S3). In the TGA trace of the as-synthesized *p*-MOF under  $\text{N}_2$  atmosphere (Fig. S4), the four coordinating DMF molecules per formula ( $[\text{Co}_3(\text{BDC})_3(\text{DMF})_4]_n$ ) were removed over the range 80-350 °C, and decomposition of *p*-MOF ensued above ~440 °C.

Rod-shaped MOF (*r*-MOF) crystals of  $[\text{Co}(\text{BDC})(\text{DMSO})]_n$  were prepared by heating a solution of  $\text{Co}(\text{NO}_3)_2 \cdot 6\text{H}_2\text{O}$  and  $\text{H}_2\text{BDC}$  in a mixture of DMF and DMSO at 120 °C. Fig. 2 shows the crystallographic structure of *r*-MOF, which has same coordination mode as  $[\text{Co}(\text{BDC})(\text{DMF})]_n$  reported by Yaghi group, except for the presence of coordinating solvent molecules.<sup>25</sup> *r*-MOF has two crystallographically independent cobalt atoms in distorted octahedral coordination geometries. Each of the  $\text{Co}^{2+}$  ions are coordinated by six oxygen atoms, of which four are provided by the BDC ligands while two are provided by DMSO molecules (Fig. 2a and Fig. S5). The infinite metal-ligand coordination generates one-dimensional

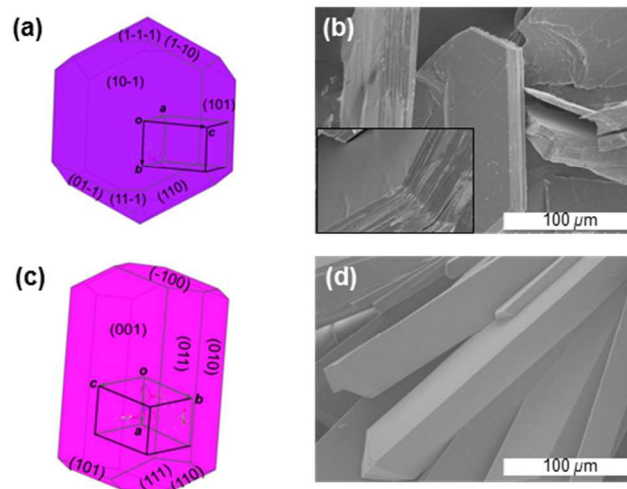


**Fig. 3** (a) Simulated crystal morphology and crystallographic facets of *p*-MOF, and (b) a SEM image of the actual crystals. (c) Simulated crystal morphology and crystallographic facets of *r*-MOF, and (d) a SEM image of the actual crystals.

Co-O chains along the *a* axis, which are bridged with four neighboring chains by BDC ligands in four different directions to form a 3D framework (Fig. 2b). The XRPD pattern of *r*-MOF was coincident with the simulated pattern (Fig. S6). In the TGA trace of the as-synthesized *r*-MOF (Fig. S7), the single coordinating DMSO molecule per formula unit ( $[\text{Co}(\text{BDC})(\text{DMSO})]_n$ ) is liberated between 250 °C and 330 °C, and decomposition of *r*-MOF occurs above ~500 °C.

To understand the different crystal shapes of *p*- and *r*-MOF, their crystal morphologies were simulated using the Bravais-Friedel-Donnay-Harker (BFDH) model with single crystal X-ray diffraction data.<sup>26</sup> As shown in Fig. 3a, the (10-1) plane of *p*-MOF corresponding to a 2D layer is placed on the board side of the crystal, and the layers are stacked in the [101] direction, parallel to the thinnest edge of the crystal. Thus, the actual crystal morphology of *p*-MOF shows good agreement with the simulation results as evidenced by scanning electron microscope (SEM) images (Fig. 3b); due to the weak interaction between layers, the plates easily flake off (Fig. 3b, inset). In a similar way, the simulated crystal morphology of *r*-MOF shows the same rod-type structure as was observed experimentally (Figs. 3c and d). The SBU of Co-O chains oriented along the *a* axis run parallel to the longest edge of the crystal, resulting in their elongated rod-shape.

We then investigated the pseudomorphic conversion reactions of Co-MOFs into cobalt oxides. Based on the TGA results, *p*-MOF was first heated under  $\text{N}_2$  (g) flow of  $50 \text{ mL min}^{-1}$  at 440 °C and maintained at this temperature for 24 h. The XRPD pattern of the resultant material enabled our identification of its structure as a mixture of cubic cobalt metal and cubic cobalt monoxide (CoO), which is coincident with JCPDS file Nos. 71-4651 and 65-2902, respectively (Fig. S8). To generate cobalt oxide with higher oxidation state,  $\text{Co}_3\text{O}_4$ ,

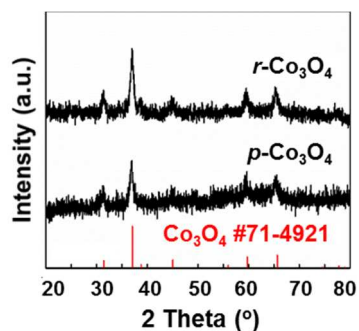


**Fig. 4** XRPD patterns of *p*- and *r*-Co<sub>3</sub>O<sub>4</sub> and JCPDS file of Co<sub>3</sub>O<sub>4</sub> as a reference.

which has a higher theoretical battery capacity of 890 mAh g<sup>-1</sup>, we carried out sequential heat treatments under an oxidizing environment.<sup>8</sup> The second pyrolysis step under O<sub>2</sub> (g) flow of 0.1 L min<sup>-1</sup> at 350 °C for 1 h successfully afforded pure Co<sub>3</sub>O<sub>4</sub> (Figs. 4 and S8). Similarly, *r*-MOF was converted to pure phase of Co<sub>3</sub>O<sub>4</sub> with an initial heat treatment under N<sub>2</sub> (g) flow of 50 mL min<sup>-1</sup> at 500 °C, followed by a second pyrolysis step under O<sub>2</sub> (g) flow of 0.1 L min<sup>-1</sup> at 500 °C for 1 h (Figs. 4 and S9). The XRPD patterns of the Co<sub>3</sub>O<sub>4</sub> indicated that the MOF-driven resultant solids corresponded to the single-phase cubic Co<sub>3</sub>O<sub>4</sub> with JCPDS file no. 71-4921. The elemental analysis revealed that no organic residue remained within both plate-shaped and rod-shaped Co<sub>3</sub>O<sub>4</sub> samples.

The textural properties of *p*- and *r*-Co<sub>3</sub>O<sub>4</sub>, such as primary nanoparticles, second structures, and tertiary architectures were carefully investigated by SEM and TEM (Fig. 5). A comparison of SEM images depicting tertiary architectures of *p*- and *r*-Co<sub>3</sub>O<sub>4</sub> show the same morphologies as those of the parent MOFs, revealing that this process is a pseudomorphic conversion (Figs. 3b and d, and Figs. 5a and c). Since organic components in MOFs are decomposed and liberated from the solid crystals during conversion, cracks on the crystal surfaces

were observed, but the external plate-like and rod-like morphologies remained. High magnification SEM and TEM images provide detailed structural information for *p*-Co<sub>3</sub>O<sub>4</sub> and *r*-Co<sub>3</sub>O<sub>4</sub>. As shown in TEM images (Figs. 5b and e), primary particles of Co<sub>3</sub>O<sub>4</sub> in both materials are observed as ca. 10 nm-sized nanocrystals, which are in agreement with the results estimated by applying the Debye-Scherrer equation to the (311) reflection (diameters of 11 nm for both). Within *p*-Co<sub>3</sub>O<sub>4</sub> and *r*-Co<sub>3</sub>O<sub>4</sub> nearly identical primary particles are agglomerated to form the secondary structures (100 to 300 nm), which finally construct the macroscopic tertiary architectures (more intimate illustration is shown in Fig. S10). As shown in Figs. 5c and f, while *p*-Co<sub>3</sub>O<sub>4</sub> was composed of the secondary particles without the integrity between primary particles, the secondary particles of *r*-Co<sub>3</sub>O<sub>4</sub> were monolithically well-integrated or connected to each other. In order to assess the porosity of the *p*-Co<sub>3</sub>O<sub>4</sub> and *r*-Co<sub>3</sub>O<sub>4</sub> structures, which is determined by secondary and tertiary structures, nitrogen adsorption-desorption measurements were conducted. As shown in Fig. S11, *p*-Co<sub>3</sub>O<sub>4</sub> and *r*-Co<sub>3</sub>O<sub>4</sub> showed typical type IV isotherms with H3 hysteresis, indicating the presence of mesopores. The Brunauer-Emmett-Teller (BET) surface areas for *p*-Co<sub>3</sub>O<sub>4</sub> and *r*-Co<sub>3</sub>O<sub>4</sub> were 57 m<sup>2</sup> g<sup>-1</sup> and 12 m<sup>2</sup> g<sup>-1</sup>, and the total pore volumes were 0.28 cc g<sup>-1</sup> and 0.08 cc g<sup>-1</sup>, respectively. The porosity difference between *p*- and *r*-Co<sub>3</sub>O<sub>4</sub> is attributed to differing assemblage densities of primary Co<sub>3</sub>O<sub>4</sub> nanocrystals as mentioned above. Consequently, compared with *r*-Co<sub>3</sub>O<sub>4</sub>, the higher surface area and porosity of *p*-Co<sub>3</sub>O<sub>4</sub> imply a looser packing of nanoparticles in each plate in addition to spacing between the stacked plates. The pore size distribution curves analysed by the nonlocal density functional theory (NLDFT) algorithm also supported these explanations. While mesopores in *p*-Co<sub>3</sub>O<sub>4</sub> are broadly distributed from 2 to 26 nm, *r*-Co<sub>3</sub>O<sub>4</sub> possesses narrow pores ranging from 2 to 8 nm.

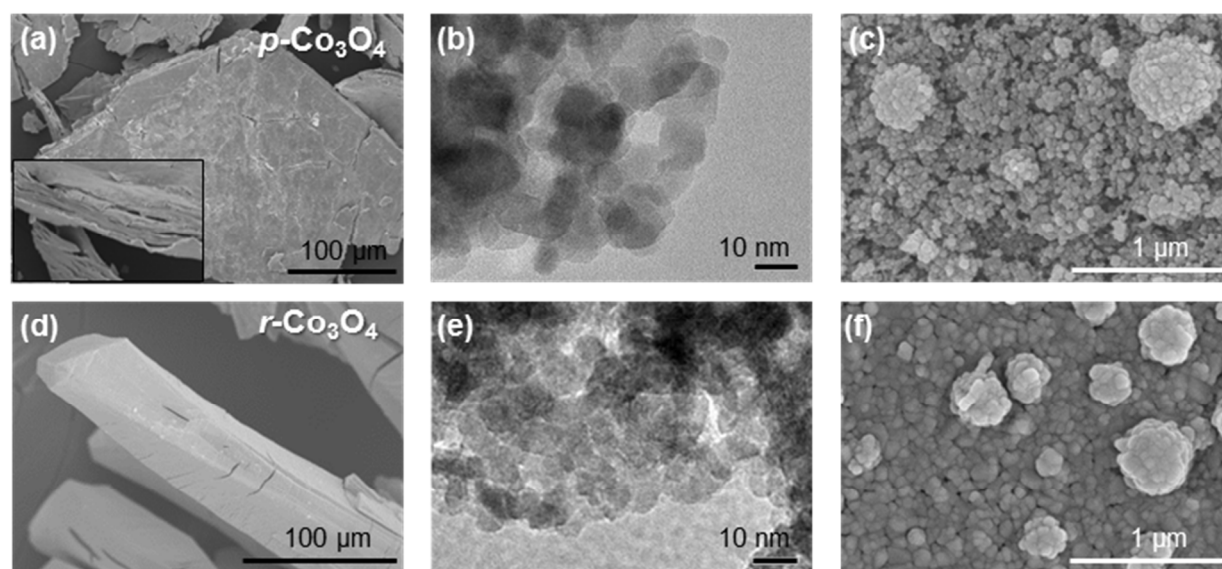


**Fig. 5** SEM and TEM images. (a) – (c) for *p*-Co<sub>3</sub>O<sub>4</sub>, and (d) – (f) for *r*-Co<sub>3</sub>O<sub>4</sub>.

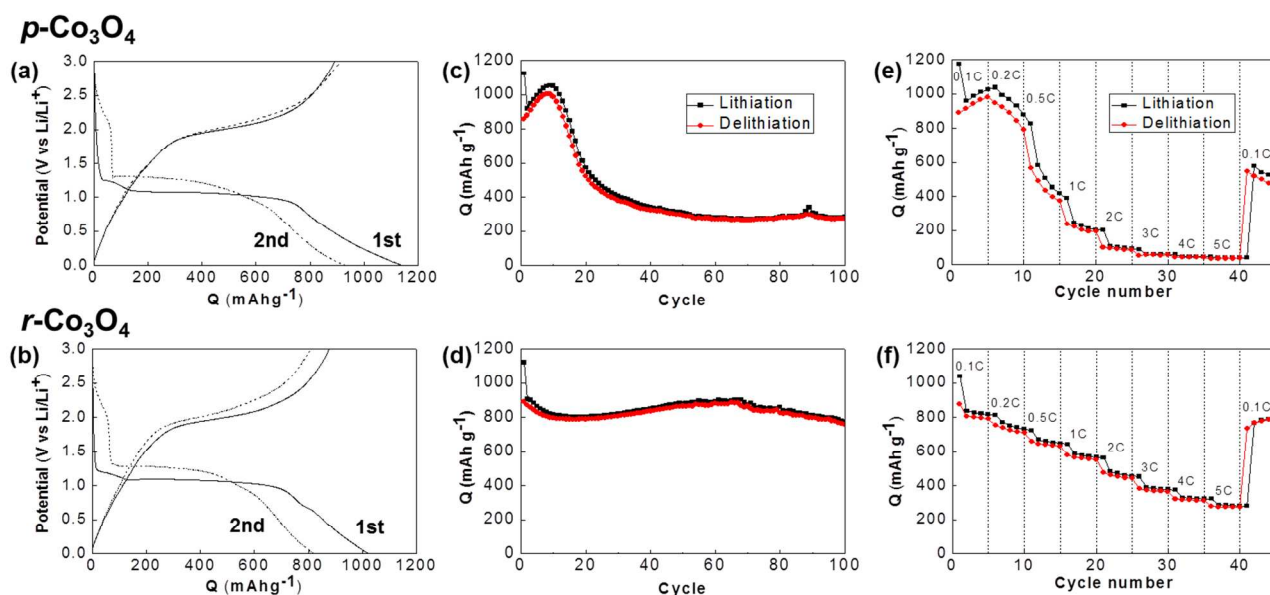


**Fig. 6** Electrochemical characteristics of  $p\text{-Co}_3\text{O}_4$  and  $r\text{-Co}_3\text{O}_4$  in the left and right columns, respectively. (a and b) Potential profiles during lithiation and delithiation at the first and second cycles. (c and d) Capacity retention during repeated cycles of charge and discharge at 0.1C for 100 cycles. (e and f) Capacity dependency on discharge rates. Charge rates were fixed at 0.1C.

The dependency of electrochemical characteristics on our  $\text{Co}_3\text{O}_4$  nanostructures was investigated (Fig. 6). As previously mentioned, the structures of our  $\text{Co}_3\text{O}_4$  can be interpreted as multi-levelled. Primary particles of around 10 nm are similar for both  $p\text{-Co}_3\text{O}_4$  and  $r\text{-Co}_3\text{O}_4$ , but in terms of their secondary and tertiary architectures, the cobalt oxides showed different degrees of assemblage as well as macroscopic shapes such as *stacked* plates or *independent* rods. Therefore, the morphological determinants of electrochemical performance can be described in terms of secondary structures and macroscopic, tertiary architectures.

Both cobalt oxides were lithiated by the same electrochemistry of the *conversion reaction*. During the initial lithiation caused by the negative potential shift, solvent molecules of electrolyte decompose to form a solid electrolyte interface (SEI) layer at 1.2 V for both  $\text{Co}_3\text{O}_4$  (Figs. 6a and b). The conversion reaction of  $\text{Co}_3\text{O}_4$  to Co metal embedded in the  $\text{Li}_2\text{O}$  matrix then proceeded at a well-defined reduction potential (1 V), which is responsible for the electrochemically reversible capacities. Additional capacities were delivered due to the pseudocapacitance of the gel-like polymer films formed at the potential-decreasing region after the conversion reactions.<sup>27</sup> Therefore, capacities of  $\text{Co}_3\text{O}_4$  have often been overestimated at values larger than the theoretical capacity of  $\text{Co}_3\text{O}_4$ , calculated only on the basis of its conversion reaction (890 mAh g<sup>-1</sup>). During the subsequent delithiation, reverse reactions proceed, including pseudocapacitance discharging and backward conversion reactions. Size-confined Co metal particles catalytically decompose  $\text{Li}_2\text{O}$  during the backward conversion reaction, forming  $\text{Co}_3\text{O}_4$ .<sup>28</sup> Therefore, a capacity loss is involved between lithiation and delithiation at the first

cycle due to the irreversible SEI formation reaction. However, the reversibility of the conversion reaction is guaranteed after the second cycle, showing coulombic efficiency higher than 95%.

Even if very similar electrochemical behaviors were observed during the initial cycles, the measured stability and kinetics of  $p\text{-}$  and  $r\text{-Co}_3\text{O}_4$  were significantly different. The  $p\text{-Co}_3\text{O}_4$  showed unstable capacity retention with a capacity increase up to the 10<sup>th</sup> cycle followed by a dramatic decrease up to 20<sup>th</sup> cycle (Fig. 6c). Conversely, its rod-shaped counterpart ( $r\text{-Co}_3\text{O}_4$ ) was observed to be much more stable, providing an enhanced cyclability (Fig. 6d):  $\sim 800$  mAh g<sup>-1</sup> with  $r\text{-Co}_3\text{O}_4$  versus less than 300 mAh g<sup>-1</sup> with  $p\text{-Co}_3\text{O}_4$  at the 100<sup>th</sup> cycle. In addition to the cycle stability, the kinetics of the conversion reaction of  $r\text{-Co}_3\text{O}_4$  was superior to that of  $p\text{-Co}_3\text{O}_4$  (Figs. 6e and f). The plate-shaped cobalt oxide did not deliver a meaningful capacity at discharge rates faster than 2C: less than 100 mAh g<sup>-1</sup> with  $p\text{-Co}_3\text{O}_4$  versus  $\sim 400$  mAh g<sup>-1</sup> with  $r\text{-Co}_3\text{O}_4$  at 2C. In terms of capacity recovery after rate-variable tests, the rod-shaped oxides were also favored, showing the same capacity at 0.1C.

Difference of cyclability and rate capability is attributed to the different architectures at higher levels in  $p\text{-}$  and  $r\text{-Co}_3\text{O}_4$  as identified by microscopies and nitrogen sorption studies previously (also see Fig. S12). During the conversion reaction, gel-like polymers are formed around metal/ $\text{Li}_2\text{O}$  nanoparticles. The insulating polymer layers could isolate the active mass from electric pathways if the oxide particles were not interconnected.<sup>29</sup>  $p\text{-Co}_3\text{O}_4$  is considered to be the case. However, the interconnected network of active mass in  $r\text{-Co}_3\text{O}_4$  (pseudo-monolithic structure) prevents the isolation from

electric pathways. The importance of the pseudo-monolithic integrity for stable and kinetically fast performances is supported by other works. Cyclability of nanoparticulate metal oxides was inferior to that of microsized counterparts.<sup>29,30</sup> Lu *et al.* showed that the electrochemical performances, especially cyclability, were improved as Co<sub>3</sub>O<sub>4</sub> particles were monolithically integrated from a physical agglomerate to nano-clusters and further macro-porous platelets.<sup>31</sup> In addition to the reason mentioned above in terms of the primary and secondary levels of morphology, there is every possibility that the spacing between stacked plates in *p*-Co<sub>3</sub>O<sub>4</sub> (as the tertiary-level structure) provide reaction surface on which the gel-like polymer layers are formed during lithiation. A macroscopic portion of plates located within the body of stacks could be isolated from electric pathways due to development of the insulating polymer films because the inner plates are not the pseudo-monolithic extension of exterior plates.

## Conclusions

In conclusion, we successfully synthesized two kinds of Co<sub>3</sub>O<sub>4</sub> nanomaterials through pseudomorphic conversion of two Co-based MOFs, which are constructed with same building blocks. Both Co<sub>3</sub>O<sub>4</sub> nanomaterials are composed of almost identical 10 nm-sized primary nanocrystals, but those nanoporous secondary structures and macroscopic morphologies such as plate and rod shapes are different, respectively. These different higher level architectures of Co<sub>3</sub>O<sub>4</sub> were examined by nitrogen sorption, TEM, and SEM analyses. *p*- and *r*-Co<sub>3</sub>O<sub>4</sub> materials were utilized as an electrode of LIB, and their electrochemical properties were comparatively studied. It was revealed that the different cyclability and rate capability is attributed to their different microstructures. Present study can provide the idea of development of electrode materials in LIBs from the point of view of higher level architectures.

## Acknowledgements

We acknowledge financial support from the Korea CCS R&D Center (KCRC) grant funded by the Korea government (Ministry of Science, ICT & Future Planning) (NRF-2013M1A8A1039968) and Basic Science Research Program through the National Research Foundation of Korea (NRF) funded by the Ministry of Education, Science and Technology (NRF-2013R1A1A3010846). This work was also supported by MOTIE (Star: 20135020900030), Korea. J.H.L. acknowledges the Global PhD Fellowship (NRF-2013H1A2A1033501). The authors acknowledge PAL for beamline use (Grant 2014-1st-2D-006).

## Notes and references

<sup>a</sup> Department of Chemistry, Ulsan National Institute of Science and Technology (UNIST), 50 UNIST-gil, Ulsan 689-798, Republic of Korea. Fax: 82-52-217-2928; Tel: 82-52-217-2019; E-mail: hoirimoon@unist.ac.kr

<sup>b</sup> Department of Energy Engineering and Department of Chemical Engineering, Ulsan National Institute of Science and Technology (UNIST), 50 UNIST-gil, Ulsan 689-798, Republic of Korea. E-mail: philiphobi@hotmail.com

† Electronic Supplementary Information (ESI) available: X-ray crystallographic data, XRPD pattern, TGA, and nitrogen sorption data for Co-MOFs. CCDC 1000305 and 1000296 for *p*-MOF and *r*-MOF,

respectively. For ESI and crystallographic data in CIF or other electronic format see DOI: 10.1039/b000000x/

‡ These authors contributed equally to this work.

- 1 D. J. Tranchemontagne, J. L. Mendoza-Cortés, M. O’Keeffe and O. M. Yaghi, *Chem. Soc. Rev.*, 2009, **38**, 1257.
- 2 H. Furukawa, K. E. Cordova, M. O’Keeffe and O. M. Yaghi, *Science*, 2013, **341**, 1230444.
- 3 L. J. Murray, M. Dincă and J. R. Long, *Chem. Soc. Rev.*, 2009, **38**, 1294.
- 4 T. A. Makal, J.-R. Li, W. Lu and H.-C. Zhou, *Chem. Soc. Rev.*, 2012, **41**, 7761.
- 5 S. Pramanik, C. Zheng, X. Zhang, T. J. Emge and J. Li, *J. Am. Chem. Soc.*, 2011, **133**, 4153.
- 6 A. Corma, H. García and F. X. Llabrés i Xamena, *Chem. Rev.*, 2010, **110**, 4606.
- 7 (a) T. K. Kim, K. J. Lee, J. Y. Cheon, J. H. Lee, S. H. Joo and H. R. Moon, *J. Am. Chem. Soc.*, 2013, **135**, 8940. (b) J. H. Lee, Y. J. Sa, T. K. Kim, H. R. Moon and S. H. Joo, *J. Mater. Chem. A*, 2014, Accepted Manuscript (DOI: 10.1039/c4ta01272k).
- 8 (a) L. Zhang, H. B. Wu and X. W. Lou, *J. Am. Chem. Soc.*, 2013, **135**, 10664. (b) L. Zhang, H. B. Wu, S. Madhavi, H. H. Hng and X. W. Lou, *J. Am. Chem. Soc.*, 2012, **134**, 17388. (c) Zhang, H. B. Wu, R. Xu and X. W. Lou, *CrystEngComm*, 2013, **15**, 9332. (d) H. B. Wu, S. Y. Wei, L. Zhang, R. Xu, H. H. Hng and X. W. Lou, *Chem. Eur. J.*, 2013, **19**, 10804.
- 9 X. Xu, R. Cao, S. Jeong and J. Cho, *Nano. Lett.*, 2012, **12**, 4988.
- 10 A. Banerjee, U. Singh, V. Aravindan, M. Srinivasan and S. Ogale, *Nano Energy*, 2013, **2**, 1158.
- 11 B. Liu, X. Zhang, H. Shioyama, T. Mukai, T. Sakai and Q. Xu, *J. Power Sources*, 2010, **195**, 857.
- 12 M.-H. Lee, J.-Y. Kim and H.-K. Song, *Chem. Commun.*, 2010, **46**, 6795.
- 13 T.-H. Kim, H.-S. Park, M.-H. Lee, S.-Y. Lee and H.-K. Song, *J. Power Sources*, 2012, **210**, 1.
- 14 Y. Lu, Y. Wang, Y. Zou, Z. Jiao, B. Zhao, Y. He and M. Wu, *Electrochem. Commun.*, 2010, **12**, 101.
- 15 X. Wang, H. Guan, S. Chen, H. Li, T. Zhai, D. Tang, Y. Bando and D. Golberg, *Chem. Commun.*, 2011, **47**, 12280.
- 16 A. J. Arvai and C. Nielsen, *ADSC Quantum-210 ADX program*; Area Detector System Corp.; Poway, CA, 1983.
- 17 *Fit2D* program: Andy Hammersley (e-mail: hammersley@esrf.fr), ESRF, 6 rue Jules Horowitz, BP 220, 38043 Grenoble Cedex 9, France.
- 18 Z. Otwinowski, W. Minor, In *Methods in Enzymology*; C. W. Carter, Jr., Sweet, R. M., Eds.; Academic Press: New York, 1997; Vol. 276, Part A, p 307.
- 19 *RapidAuto* software, version 2.40; Rigaku Corp.: Tokyo, Japan.
- 20 G. M. Sheldrick, *SHELXL-97, Program for the Solution of Crystal Structures*, University of Göttingen, Göttingen, Germany, 1997.
- 21 G. M. Sheldrick, *SHELXL-PLUS, Crystal Structure Analysis Package*; Bruker Analytical X-ray: Madison, WI, 1997.
- 22 F. Luo, Y. Che and J. Zheng, *Cryst. Growth Des.*, 2009, **9**, 1066.
- 23 X.-F. Wang, Y.-B. Zhang, W. Xue, X.-L. Qi and X.-M. Chen, *CrystEngComm.*, 2010, **12**, 3834.

- 24 R. D. Poulsen, A. Bentien, M. Christensen and B. B. Iversen, *Acta Cryst.*, 2006, **B62**, 245.
- 25 N. L. Rosi, J. Kim, M. Eddaoudi, B. Chen, M. O'Keeffe and O. M. Yaghi, *J. Am. Chem. Soc.*, 2005, **127**, 1504.
- 26 (a) A. Bravais, *Etudes Cristallographiques*; Gauthier Villars: Paris, 1866. (b) G. Friedel, *Bull. Soc. Franc. Mineral.*, 1907, **30**, 326. (c) J. D. H. Donnay and D. Harker, *Am. Mineral.*, 1937, **22**, 463.
- 27 S. Laruelle, S. Grugeon, P. Poizot, M. Dolle, L. Dupont and J-M. Tarascon, *J. Electrochem. Soc.*, 2002, **149**, A627.
- 28 P. Poizot, S. Laruelle, S. Grugeon, L. Dupont and J-M. Tarascon, *Nature*, 2000, **407**, 496.
- 29 F. Jiao, J. Bao and P. G. Bruce, *Electrochem. Solid-State Lett.*, 2007, **10**, A264.
- 30 Y. X. Chen, L. H. He, P. J. Shang, Q. L. Tang, Z. Q. Liu, H. B. Liu and L. P. Zhou, *J. Mech. Sci. Technol.*, 2011, **27**, 41.
- 31 Y. Lu, Y. Wang, Y. Zou, Z. Jiao, B. Zhao, Y. He and M. Wu, *Electrochem. Commun.*, 2010, **12**, 101.

## ARTICLE

**TOC Graphic****Preparation of  $\text{Co}_3\text{O}_4$  electrode materials with different microstructures *via* pseudomorphic conversion of Co-based metal-organic frameworks**

Kyung Joo Lee, Tae-Hee Kim, Tae Kyung Kim, Jae Hwa Lee, Hyun-Kon Song,\* and Hoi Ri Moon\*



Pseudomorphic conversion of MOFs resulted in the controlled preparation of  $\text{Co}_3\text{O}_4$  nanoparticles with different microstructures, which showed different electrochemical properties.